CrossMark

TECHNICAL ARTICLE

Crystallographic characterization of fluorapatite glass-ceramics synthesized from industrial waste

Chee W. Loy,[1] Khamirul A. Matori,[2] Norhazlin Zainuddin,[3] Andrew E. Whitten,[4] Christine Rehm,[4] Liliana de Campo,[4] Anna Sokolova,[4] and Siegbert Schmid[1,a)]
[1]*School of Chemistry, The University of Sydney, Sydney NSW 2006, Australia*
[2]*Department of Physics, Universiti Putra Malaysia, UPM Serdang 43400, Malaysia*
[3]*Department of Chemistry, Universiti Putra Malaysia, UPM Serdang 43400, Malaysia*
[4]*Australian Centre for Neutron Scattering, Australian Nuclear Science and Technology Organisation, Lucas Heights, NSW 2234, Australia*

(Received 28 April 2017; accepted 4 July 2017)

A series of phase transformations of a novel fluoroaluminosilicate glass forming a range of fluorapatite glass-ceramics on sintering are reported. The sintering process induces formation of fluorapatite, mullite, and anorthite phases within the amorphous silicate matrices of the glass-ceramics. The fluoroaluminosilicate glass, SiO_2–Al_2O_3–P_2O_5–CaO–CaF_2, is prepared from waste materials, such as rice husk ash, pacific oyster shells, and disposable aluminium cans. The thermally induced crystallographic and microstructure evolution of the fluoroaluminosilicate glass towards the fluorapatite glass-ceramics, with applications in dental and bone restoration, are investigated by powder X-ray diffraction and small-angle neutron-scattering techniques. © *2017 International Centre for Diffraction Data.*
[doi:10.1017/S088571561700094X]

Key words: fluorapatite, mullite, anorthite, spinodal decomposition, glass-ceramic

I. INTRODUCTION

Apatite-based glass-ceramics have been extensively studied in recent decades. They show excellent mechanical properties, bioactivity, and compatibility for biomedical applications (Wolfe and Boyde, 1992). They can form an apatite layer and strong chemical bonds at the bone or tooth interface with the implant (Denry and Holloway, 2014). The nanocrystalline structures, bioactivity, and mechanical strengths of the glass-ceramics depend on their parent glass composition and the crystallization processes during sintering (Nayak and Bera, 2010; O'Donnell *et al*., 2010; Dessai *et al*., 2013).

Fluorapatite has the formula $Ca_{10}(PO_4)_6F_2$ and hexagonal crystal symmetry with space group $P6_3/m$. It has chemical and crystallographic similarities with the hydroxyapatite phase, $Ca_{10}(PO_4)_6(OH)_2$, which is the main natural bone mineral (Denry and Holloway, 2014). The fluorine content in the fluoroaluminosilicate glass plays an important role in lowering the cross-link density of the glass, facilitating particle kinetics for crystallization, and promoting bulk nucleation of fluorapatite (Rafferty *et al*., 2000). Crystallization of a fluoroaluminosilicate glass leads to a fluorapatite glass-ceramic. The presence of the fluorapatite phase in a glassy matrix further improves the biocompatibility and hardness of the parent glass. Sintering of fluoroaluminosilicate glasses often induces the formation of mullite and anorthite phases. These phases can improve the mechanical and thermal properties of the glass-ceramic (O'Donnell *et al*., 2010).

Small-angle neutron scattering (SANS) is a powerful tool to study the crystallization processes involved in the formation of fluorapatite glass-ceramics, such as spinodal decomposition, amorphous phase separation, nucleation, and growth (Duminis *et al*., 2017). The crystallization process causes phase separation and local compositional changes in the glass sample. In a SANS experiment, neutron scattering occurs when neutrons interact with the interface between phases, each with its own nuclear contrast. In general, the nucleation and growth of crystalline fluorapatite exhibits increasing neutron-scattering intensity at low wave vector, Q (<0.01 $Å^{-1}$), because of the increasing size of the crystallite. Crystallization of the fluorapatite phase because of spinodal decomposition results in a shoulder in the neutron-scattering profile at higher Q (0.01–0.05 $Å^{-1}$) and shifts to lower Q at higher temperatures (Hill and Calver, 2007).

II. EXPERIMENTAL

A. Sample preparation

The raw materials for the study were sourced from waste materials such as rice husk ash, pacific oyster shells, and disposable aluminium cans. Rice husk ash from the species of *Oryza sativa* L. was utilized as a source of SiO_2 (Srinivasreddy *et al*., 2013). We used an agricultural waste product from the Chit Serm Thai Ricemill Co., Ltd (Thailand). The rice husk ash was re-heated at 800 °C before being used in the glass formulation. Pacific oyster shells (*Crossostrea gigas*) originating from the Tasman Sea were collected from Australian seafood waste as a source of $CaCO_3$. The shells were cleaned with water, dried, calcined at 400 °C for 3 h, and then ground into powder. Disposable aluminium cans from Sydney urban waste were sampled as a source of Al_2O_3. The aluminium cans were dissolved in 1.0 M sodium hydroxide solution and aluminium hydroxide was

a)Author to whom correspondence should be addressed. Electronic mail: siegbert.schmid@sydney.edu.au

Downloaded from https://www.cambridge.org/core, subject to the Cambridge Core terms of use.

TABLE I. Raw materials for the synthesis of fluoroaluminosilicate glass

Components of fluoroaluminosilicate glass	Weight percentage (%)
Rice husk ash	25.4
Pacific oyster shell powder	23.0
Alumina from disposable aluminium cans	23.4
CaF_2 (Alfa Aesar, 99.95%, metal basis)	11.9
P_4O_{10} (Alfa Aesar, 99.99%, metal basis)	16.3

precipitated by carbon dioxide. The precipitate was dried and then calcined at 600 °C for 3 h. Recycling disposable aluminium cans by this method is simple and environmental friendly. The precipitation process has a potential to be applied as carbon dioxide capture and storage to reduce greenhouse gas emissions. It also supports the objective of the United Nations Framework Convention on Climate Change (UNFCCC) to stabilize greenhouse gas concentrations in the atmosphere at a level that will prevent dangerous anthropogenic interference with the climate system (Dixon *et al*., 2013).

A fluoroaluminosilicate glass was prepared by melting its constituent components (Table I) in a round-bottom alumina crucible at 1450 °C and then casting the content into water at room temperature. The glass composition was formulated with a Ca:P:F ratio of 5:3:4. A glass with high fluorine content and Ca/P ratio of 1.67 (apatite stoichiometry) is favourable for fluorapatite bulk nucleation (Rafferty *et al*., 2000; Duminis *et al*., 2017). Our study of the crystallization of fluoroaluminosilicate glass involved in the formation of glass-ceramics is performed using sintered samples quenched to room temperature. The fluoroaluminosilicate glass frit collected from the casting was ground into powder form (<45 μm) by high-energy ball milling, and then pressed into pellets. These were sintered at 700, 800, 900, 1000 or 1100 °C for 3 h. For powder X-ray diffraction (PXRD) and SANS characterization, the pellets were ground into powder by hand using an agate mortar and pestle.

B. Data collection and analysis

PXRD measurements were performed using a PANalytical X'Pert Pro multipurpose diffractometer with a Philips PW3040/60 X-ray generator and PIXcel detector. Monochromatic Cu$K\alpha$ X-ray radiation with a wavelength of 1.5406 Å was used for the experiments. The X-ray diffraction data were collected from $10° \leq 2\theta \leq 90°$ with a step size of 0.01313°. Powder samples were flattened on a zero background silicon disc for the X-ray diffraction measurements.

Time-of-flight SANS measurements were performed at the Bilby instrument of the Australian Centre for Neutron Scattering at ANSTO (Sokolova *et al*., 2016). The Bilby instrument uses four choppers to produce neutron pulses with wavelengths of 2–18 Å (with a wavelength resolution, $\Delta\lambda/\lambda$, of ~10%) for the small-angle scattering data collection. The instrument was configured with a circular source aperture with diameter of 40 mm, a circular sample aperture with a diameter of 12.5 mm, and a collimation length of ~16.5 m. Two independent detector carriages were positioned at a sample-to-detector distance of ~18.0 and ~4.0 m, respectively. A fluorapatite glass-ceramic and its parent glass powder samples were each prepared in a demountable sample cell of 0.1 mm thickness and covered by two quartz windows. The spacing between the powder particles was filled by a mixture of H_2O–D_2O solvent (75 wt% D_2O). The H_2O–D_2O solvent has a similar neutron scattering length density as the parent glass phase. The purpose of using the H_2O–D_2O solvent is to reduce the scattering from voids and to contrast match the parent glass phase. Hence, any structural or compositional changes in the glass-ceramic relative to its parent glass will cause contrast differences and lead to changes in the SANS curve. The intensity of scattered neutrons between $0.0012 < Q < 0.39$ Å^{-1} was measured for 30 min per sample. Data were reduced using the Mantid software (Arnold *et al*., 2014) and analysed using SasView 3.1.2 (http://www.sasview.org).

III. RESULTS AND DISCUSSION

Figures 1–3 show the PXRD patterns of rice husk ash, pacific oyster shell powder, and alumina from disposable aluminium cans, respectively. The PXRD results revealed that the SiO_2 from the rice husk ash was amorphous, while the pacific oyster shell powder consisted of crystalline $CaCO_3$ with trigonal symmetry (calcite). The alumina synthesized from

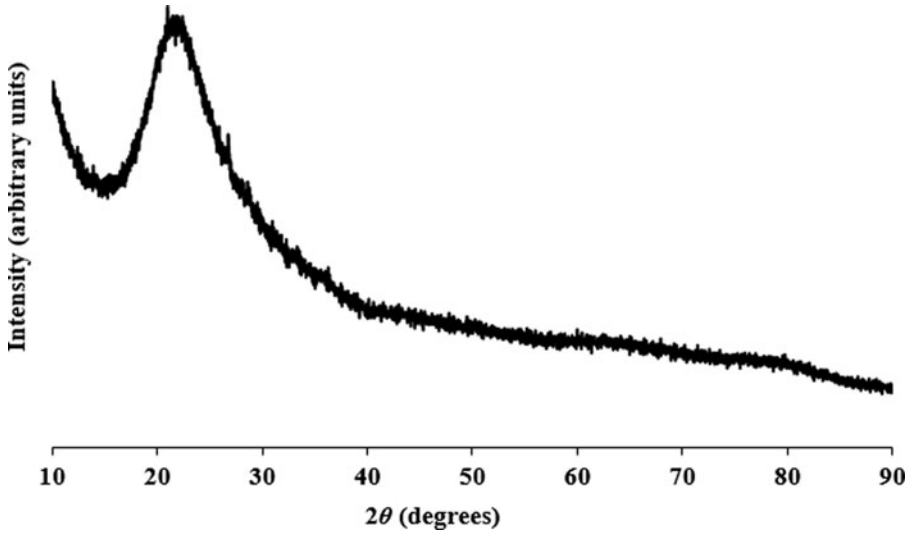

Figure 1. PXRD pattern for rice husk ash powder from Thailand collected at $\lambda = 1.5406$ Å.

Downloaded from https://www.cambridge.org/core, subject to the Cambridge Core terms of use.

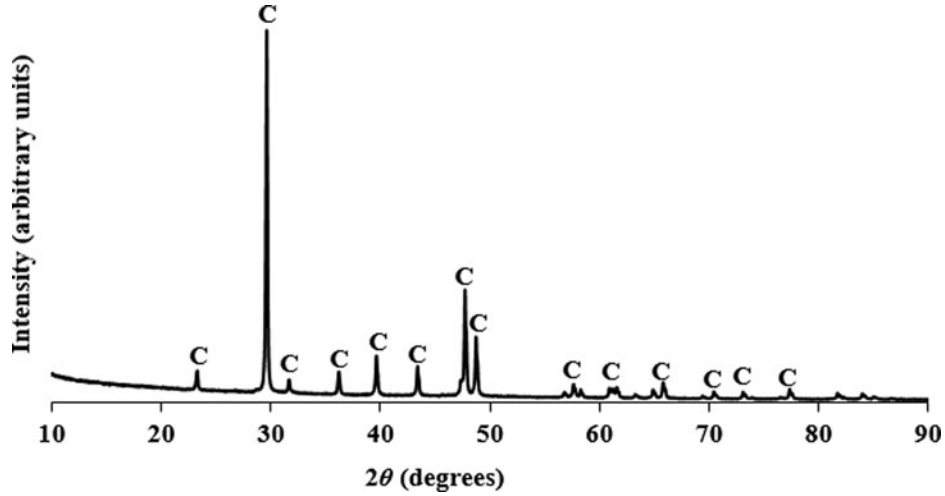

Figure 2. PXRD pattern for pacific oyster shell powder from the Tasman Sea collected at $\lambda = 1.5406$ Å (C represents the diffraction peaks of calcite).

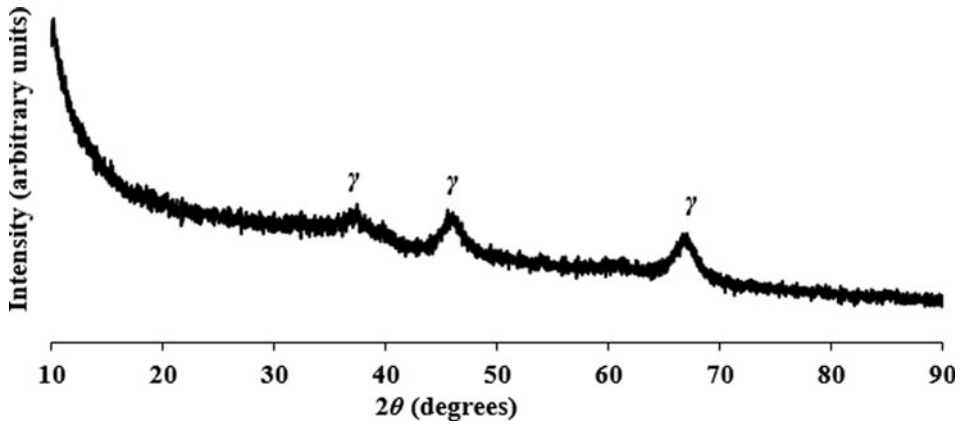

Figure 3. PXRD pattern for alumina powder synthesized from disposable aluminium cans collected at $\lambda = 1.5406$ Å (γ represents the diffraction peaks of short range ordered γ-alumina).

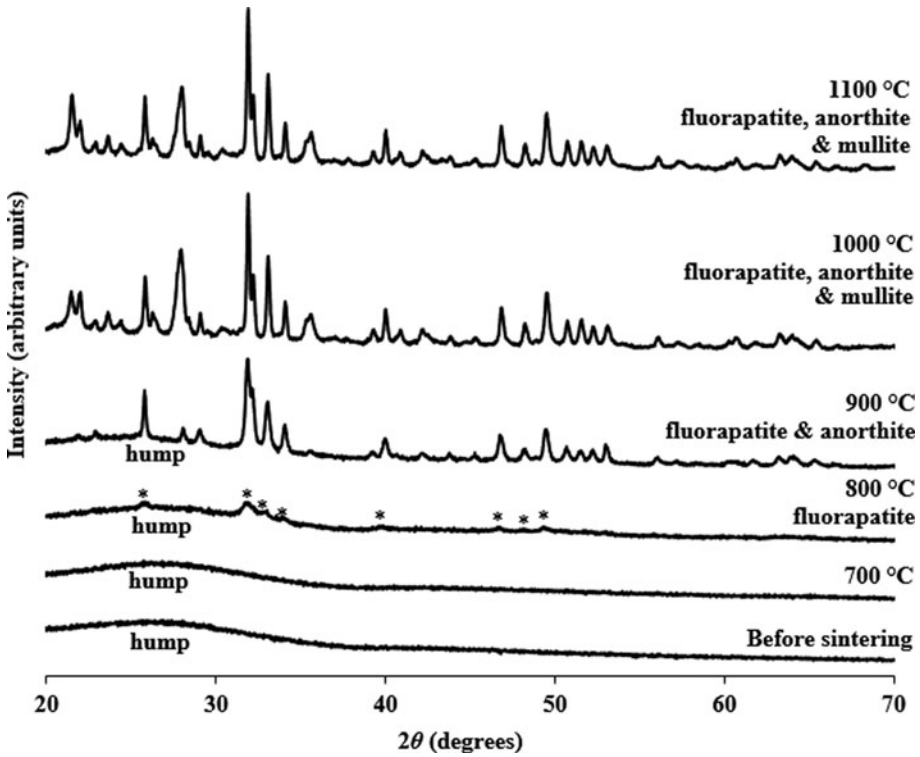

Figure 4. PXRD patterns for fluoroaluminosilicate glass before and after sintering at 700, 800, 900, 1000 and 1100 °C, respectively, collected at $\lambda = 1.5406$ Å (*represents the diffraction peaks of fluorapatite phase).

Downloaded from https://www.cambridge.org/core, subject to the Cambridge Core terms of use.

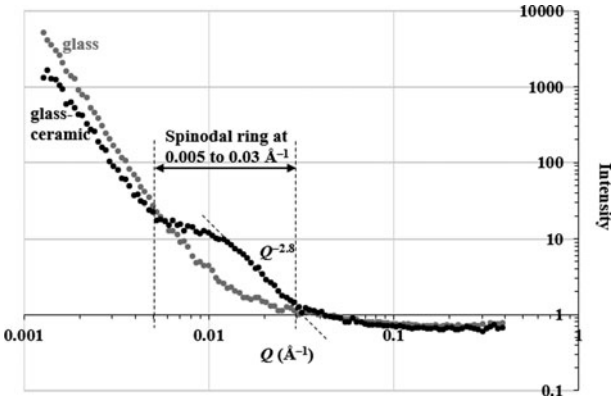

Figure 5. SANS profiles of fluoroaluminosilicate glass and fluorapatite glass-ceramic synthesized at 900 °C.

disposable aluminium cans consisted of short range ordered γ-Al_2O_3. The synthesis involved the reaction of aluminium with aqueous sodium hydroxide to form a sodium aluminate solution. Carbonation of this solution induced crystallization of pseudoboehmite. Subsequent dehydration of pseudoboehmite at 600 °C resulted in the short range ordered γ-Al_2O_3.

The fluoroaluminosilicate glass frit was optically clear. Figure 4 shows the PXRD patterns of the fluoroaluminosilicate glass powder before and after sintering. The pattern of the fluoroaluminosilicate glass before sintering shows a wide hump at $20° < 2\theta < 36°$ consistent with the glassy nature of the SiO_2–Al_2O_3–P_2O_5–CaO–CaF_2 system (Denry and Holloway, 2014). The rapid cooling of the melt from 1450 °C to room temperature, via water-quenching technique, lead to the formation of a short-range ordered glass.

The fluoroaluminosilicate glass particles remained in an amorphous phase after sintering at 700 °C. Diffraction peaks for the fluorapatite phase began to appear at ~800 °C and the fluorapatite glass-ceramic is formed after sintering its parent glass at ≥ 800 °C for 3 h. The corresponding diffraction peaks were weak and wide. This reveals that the fluorapatite phase has small crystallite size and slow bulk nucleation or spinodal decomposition rate. After sintering at 900 °C, the diffraction peaks for the fluorapatite phase are well defined. The formation of the fluorapatite phase because of spinodal decomposition causes the surrounding glass phase to undergo depletion in Ca, P, and F concentration. As a result, the resulting glass phase consists of Ca/P/F-rich and Si/Al-rich glass regions. The concentration changes gradually from Ca/P/F-rich glass to Al/Si-rich glass. The growth of the fluorapatite phase leaves insufficient Ca and P species to charge balance the Al/Si-rich site. The fourfold coordination of tetrahedral aluminium in the glass network becomes unstable and transforms to octahedral aluminium with the sixfold coordination. As a result, anorthite forms as a minor phase in the glass-ceramic. The anorthite may form by heterogeneous surface nucleation and bulk nucleation at the Al/Si-rich sites of the glass phase.

After sintering at 1000 °C, the diffraction peaks of both fluorapatite and anorthite became more intense and narrower, confirming that both phases were more crystalline. Mullite also begins to crystallize at ~1000 °C and the amorphous hump, which was present for lower temperature sintering, disappeared. The high concentration of octahedral aluminium and tetrahedral silicon cations in the Al/Si-rich glass regions induced the nucleation of mullite. The fluorapatite, mullite, and anorthite phases have higher crystallinity after sintering the parent glass at 1100 °C.

Figure 5 shows the SANS profiles for the fluoroaluminosilicate glass and a fluorapatite glass-ceramic (synthesized by sintering its parent glass at 900 °C for 3 h) in 75%-D_2O. The neutron scattering intensity of the glass-ceramic at low $Q < 0.005$ Å^{-1} is decreased relative to the parent glass. This indicates that the glass-ceramic does not undergo phase separation by a binodal mechanism and there is no large nucleated fluorapatite structure at the length scale of >1250 Å (Hill and Calver, 2007). A wide shoulder or "spinodal ring" appeared in the neutron-scattering curve of the glass-ceramic at $0.005 < Q < 0.03$ Å^{-1} indicating that the early stage of spinodal decomposition occurs at the length scale of 200–1250 Å (Hill and Calver, 2007). The Guinier–Porod model was applied to fit the neutron scattering data of the glass-ceramic at $0.005 < Q < 0.39$ Å^{-1}. The result indicated that the dimensional variable in the Guinier region was $s = 0.0 \pm 0.1$, the radius of gyration was 120 ± 5 Å, and the Porod exponent was 2.9 ± 0.1. The dimensional variable indicates that the spinodal decomposed structure in the glass-ceramic has three-dimensional structure (dimensionality = $3 - s$). Assuming the crystallites are roughly spherical, the radius of gyration suggests that the size of the crystallites is ~310 Å, and a Porod exponent of ~3 is indicative of a rough or fractal surface of the spinodal decomposed structure. Figure 6 schematically

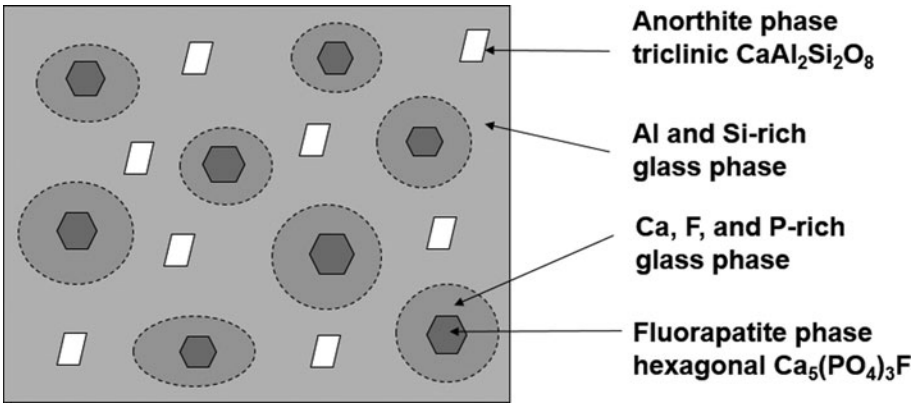

Figure 6. Schematic of crystallization of fluorapatite and anorthite phases in the glass-ceramic system.

Downloaded from https://www.cambridge.org/core, subject to the Cambridge Core terms of use.

shows the formation of the fluorapatite phase, and Ca/P/F-rich and Si/Al-rich glass regions within the spinodal decomposition region. The spinodal decomposed structure was associated with the Ca/P/F-rich glass region. Both Ca/P/F-rich and Si/Al-rich glass regions, formed by spinodal decomposition, have a high interconnectivity (Favvas and Mitropoulos, 2008). The Ca/P/F composition was gradually decreased as the distance from the fluorapatite phase increases. Hence, the early stage of crystallization of the fluorapatite phase has a large energy barrier to drive Ca, P, and F species across the Al/Si-rich glass phase. The crystallization of fluorapatite was inhibited by the formation of the Si/Al-rich glass phase. Finally, crystallization of anorthite is more favourable in the Si/Al-rich glass phase.

IV. CONCLUSION

PXRD examinations showed the crystalline phase transition of an amorphous SiO_2–Al_2O_3–P_2O_5–CaO–CaF_2-based glass to multi-functional phases of glass-ceramics after sintering at 800 and 900 °C. Sintering the glass at ≥800 °C forms a fluorapatite phase by spinodal decomposition. Crystallization of anorthite and mullite is because of the depletion of Ca and P species during formation of the fluorapatite phase. The aluminium species in the glass network changed from fourfold to sixfold coordinations to balance the depletion of Ca and P species in the Al/Si-rich glass region. At sufficiently high temperature (≥900 °C), anorthite and mullite are formed in the Al/Si-rich glass region. They can improve the mechanical and thermal properties of the glass-ceramic for implant applications.

SANS indicates the formation of fluorapatite as a result of spinodal decomposition. The data also suggest the phase separation of Al/Si-rich and Ca/P/F-rich glass regions by a spinodal mechanism leading to a gradual change in composition. Neutron scattering because of the spinodal decomposed structure (Ca/P/F-rich glass regions) appears in the scattering data at $0.005 < Q < 0.03$ Å^{-1}, and corresponds to a size of 200–1250 Å.

ACKNOWLEDGEMENTS

This work benefited from the use of the SasView application, originally developed under NSF award DMR-0520547. SasView contains code developed with funding from the European Union's Horizon 2020 research and innovation programme under the SINE2020 project, Grant No. 654000. The authors acknowledge the supply of rice husk ash by Professor T. J. McCarthy (School of Civil Mining and Environmental Engineering, University of Wollongong).

Arnold, O., Bilheux, J. C., Borreguero, J. M., Buts, A., Campbell, S. I., Chapon, L., Doucet, M., Draper, N., Ferraz Leal, R., Gigg, M. A., Lynch, V. E., Markvardsen, A., Mikkelson, D. J., Mikkelson, R. L., Miller, R., Palmen, K., Parker, P., Passos, G., Perring, T. G., Peterson, P. F., Ren, S., Reuter, M. A., Savici, A. T., Taylor, J. W., Taylor, R. J., Tolchenov, R., Zhou, W., and Zikovsky, J. (**2014**). "Mantid – data analysis and visualization package for neutron scattering and μSR experiments," Nucl. Instrum. Methods Phys. Res. **764**, 156–166.

Denry, I. and Holloway, J. A. (**2014**). "Low temperature sintering of fluorapatite glass-ceramics," Dent. Mater. **30**(2), 112–121.

Dessai, R. R., Desa, J. A. E., Sen, D., and Mazumder, S. (**2013**). "Effects of pressure and temperature on pore structure of ceramic synthesized from rice husk: a small angle neutron scattering investigation," J. Alloys Compd. **564**, 125–129.

Dixon, T., Romanak, K., Neades, S., and Chadwick, A. (**2013**). "Getting science and technology into international climate policy: carbon dioxide capture and storage in the UNFCCC," Energy Proc. **37**, 7590–7595.

Duminis, T., Shahid, S., and Hill, R. G. (**2017**). "Apatite glass-ceramics: a review," Front. Mater. **3**(59), 1-15.

Favvas, E. P. and Mitropoulos, A. Ch. (**2008**). "What is spinodal decomposition," J. Eng. Sci. Technol. Rev. **1**, 25–27.

Hill, R. and Calver, A. (**2007**). "Real-time nucleation and crystallization studies of fluorapatite glass-ceramics using small-angle neutron scattering and neutron diffraction," J. Am. Ceram. Soc. **90**(3), 763–768.

Nayak, J. P. and Bera, J. (**2010**). "Effect of sintering temperature on medical behavior and bioactivity of sol-gel synthesized bioglass-ceramics using rice husk ash as a silica source," Appl. Surf. Sci. **257**, 458–462.

O'Donnell, M. D., Karpukhina, N., Calver, A. I., Law, R. V., Bubb, N., Stamboulis, A., and Hill, R. G. (**2010**). "Real time neutron diffraction and solid state NMR of high strength apatite-mullite glass ceramic," J. Non-Cryst. Solids **356**, 2693–2698.

Rafferty, A., Clifford, A., Hill, R., Wood, D., Samuneva, B., and Dimitrova-Lukacs, M. (**2000**). "Influence of fluorine content in apatite-mullite glass-ceramics," J. Am. Ceram. Soc. **83**(11), 2833–2838.

Sokolova, A., Christoforidis, J., Eltobaji, A., Barnes, J., Darmann, F., Whitten, A. E., and Campo, L.de. (**2016**). "BILBY: time-of-flight small angle scattering instrument," Neutron News **27**, 9–13.

Srinivasreddy, A. B., McCarthy, T. J., and Lume, E. (**2013**). "Effect of rice husk ash on workability and strength of concrete," 26th Biennial Concrete Institute of Australia's National Concrete (Concrete 2013), 1–10.

Wolfe, L. A. and Boyde, A. (**1992**). "Biocompatibility test on a novel glass-ceramic system," J. Appl. Biomater. **3**, 217-224.

Downloaded from https://www.cambridge.org/core, subject to the Cambridge Core terms of use.